



1 **Spatiotemporal Heterogeneity of  $b$  Values Revealed by a**  
2 **Data-Driven Approach for June 17, 2019  $M_s$  6.0,**  
3 **Changning Sichuan, China earthquake Sequence**

4 Changsheng Jiang<sup>1\*</sup>, Libo Han<sup>1</sup>, Feng Long<sup>2</sup>, Guijuan Lai<sup>1</sup>, Fengling Yin<sup>1</sup>, Jinmeng Bi<sup>3</sup>,  
5 Zhengya Si<sup>4</sup>

6 <sup>1</sup> Institute of Geophysics, China Earthquake Administration, Beijing 100081, China

7 <sup>2</sup> Sichuan Earthquake Agency, Chengdu 610041, China

8 <sup>3</sup> Tianjin Earthquake Agency, Tianjin 300201, China

9 <sup>4</sup> Beijing Earthquake Agency, Beijing 100080, China

10 *Correspondence to:* Changsheng Jiang (jiangcs@cea-igp.ac.cn)

11 **Abstract.** The spatiotemporal heterogeneity of  $b$  values has great potential for understanding the  
12 seismogenic process and assessing the seismic hazard. However, there is still much controversy about  
13 whether it exists or not, and an important reason is that the choice of subjective parameters has eroded  
14 the foundations of many researches. To overcome this problem, we used a recent developed non-  
15 parametric method based on the data-driven concept to calculate  $b$  values. The major steps of this method  
16 include: 1) perform a large number of Voronoi tessellation, Bayesian information criterion (BIC) value  
17 calculation and selection of the optimal models for the study area, and 2) use the ensemble median ( $Q_2$ )  
18 and median absolute deviation (MAD) value to represent the final  $b$  value and its uncertainty. We  
19 investigated spatiotemporal variations of  $b$  values before and after the 2019 Changning  $M_s$  6.0 earthquake  
20 in Sichuan Basin, China. The results reveal a spatial volume with low pre-mainshock  $b$  values near the  
21 mainshock source region, and its size corresponds roughly with the rupture area of the mainshock. The  
22 anomalously high pre-mainshock  $b$  values distributed in the NE direction of the epicenter was interpreted  
23 to be related with fluid invasion or increased pore pressure. The decreases of  $b$  values during the  
24 aftershock sequence along with the occurrences of several strong aftershocks imply that  $b$  values could  
25 be an indicator of stress state. In addition, we found that although the distribution characteristics of  $b$   
26 values obtained from different way of investigating are qualitatively consistent, they differ significantly  
27 in terms of their specific values, suggesting that the best way to study the heterogeneous pattern of  $b$   
28 values is in the joint dimension of space-time rather than alone in time and space. Overall, our study  
29 emphasizes the importance of  $b$  value studies on assessing the earthquake hazards.

30 **Keywords**  $b$  value; data-driven; spatiotemporal heterogeneity; Ogata-Katsura 1993 model; Voronoi  
31 tessellation



32 **Introduction**

33 The Gutenberg-Richter  $b$  value describes the corresponding frequency-magnitude distribution (FMD)  
34 characteristics by reflecting the relative proportion of the frequency of large and small earthquakes within  
35 a given space-time range. It is considered to be related to the stress conditions in the Earth's crust (e.g.,  
36 Wyss, 1973; Urbancic et al., 1992; Mori and Abercrombie, 1997; Toda et al., 1998), complexity of the  
37 fault trace (Stirling et al., 1996), and the extent of creep (Amelung and King, 1997) and other factors.  
38 Experimental studies in the laboratory have shown that a weak and less resistant environment under  
39 stress would produce a high  $b$  value, while materials that are more compact and more resistant under  
40 pressure do not fail, which leads to a reasonable low  $b$  value (Aktar et al., 2004). In the case where the  
41 material and structure are clarified, decreasing  $b$  value is considered to be related to increasing stress  
42 (Scholz, 1968) or pore pressure diffusion (Hainzl and Fischer, 2002; Lei and Satoh, 2007). For the above  
43 reasons,  $b$  value has been widely concerned in seismogenic environment analysis and seismic hazard  
44 research.

45 Spatial and temporal heterogeneity is an important topic in  $b$  value research, especially under the  
46 assumption that the local  $b$  values are inversely dependent on the applied shear stress, and that low  $b$   
47 values ( $b < 0.7$ ) can reflect the existence of locked faults or asperities. Therefore, the spatial and temporal  
48 heterogeneity of  $b$  values is considered as an important clue for forecasting the location and size of  
49 potential large earthquakes (Wiemer and Wyss, 1997; Schorlemmer and Wiemer, 2005; Murru et al.,  
50 2007). Using the spatial heterogeneity of  $b$  value to identify possible asperities is performed in some  
51 cases, such as the San Jacinto-Elsinore fault system in southern California (Wyss et al., 2000), the  
52 Parkfield segment of the San Andreas fault (Wiemer and Wyss, 1997), and the case study of the 2014  
53 Parkfield  $M$  6.0 earthquake (Schorlemmer and Wiemer, 2005).

54 A model named Asperity Likelihood Model (ALM) based on the above assumptions has been developed  
55 and used to forecast future earthquakes (Wiemer and Schorlemmer, 2007; Gulia et al., 2010). The  
56 research on the temporal heterogeneity of  $b$  values mainly includes using  $b$  value time variation of early  
57 aftershock sequence and the constructed system of foreshock traffic light system (FTLS) to evaluate the  
58 risk of subsequent larger aftershocks (Gulia and Wiemer, 2019).

59 However, some research results show that the apparent variability of  $b$  values is not significant in some  
60 cases (Del Pezzo et al., 2003). For example, Amorèse et al. (2010) systematically examined the variation



61 of  $b$  values in Southern California to the depth of the crust, and found that the hypothesis was not  
62 statistically significant. By using a data-driven approach, Kamer and Hiemer (2015) shows that the  
63 spatial  $b$  values in most locations in California are distributed within a very limited range ( $0.94 \pm 0.04$ –  
64  $1.15 \pm 0.06$ ), and the previously reported spatial  $b$  value variation is overestimated and mainly due to the  
65 subjective choice of parameters. Besides, the spatial and temporal heterogeneity of  $b$  values is also  
66 considered to be due to the subjective arbitrariness of the calculation rules and the lack of statistical  
67 robustness (Kagan 1999).

68 Based on the above viewpoints, the calculation reliability for researches on the spatiotemporal  
69 heterogeneity of  $b$  values still needs to be solved, and the relationship between the spatiotemporal  
70 variation process of  $b$  values and the occurrence of strong earthquakes need to be found out for more  
71 earthquake cases. In this study, we will utilize data-driven based  $b$  values calculation methods that have  
72 been developed in recent years (Kamer and Hiemer, 2015; Nandan et al., 2017; Si and Jiang, 2019) for  
73 case studies of the 2019 Changning  $M_S$  6.0 earthquake in Sichuan, China.

#### 74 **Method**

75 In the traditional calculation of the Gutenberg-Richter magnitude-frequency  $b$  value, a fixed number of  
76 earthquakes (Hutton et al., 2010; Ogata, 2011) or a fixed minimum and maximum selection radius  
77 (Woessner and Wiemer, 2005) are generally used to select data and the maximum likelihood estimation  
78 is used to obtain  $b$  values. Because such calculations have strong subjectivity in calculating rules, it has  
79 caused widespread controversy. The data-driven approaches to seismicity parameter calculation have  
80 been gradually developed in recent years (Sambridge et al., 2013; Kamer and Hiemer, 2015; Nandan et  
81 al., 2017; Si and Jiang, 2019), by using the Voronoi tessellation to create a large number of spatially  
82 random grids and covering the possibility of segmentation of spatial regions, relying on the Bayesian  
83 information criterion (BIC) to select a part of the optimal models with the smallest BIC value, and  
84 representing the final result of seismic activity parameters through the ensemble median value. Because  
85 the data-driven approach uses an automatic parametric calculation, it provides a possibility for solving  
86 the subjective problem of earthquake data selection.

87 Among those data-driven approaches, Si and Jiang (2019) developed a method using continuous  
88 distribution function (hereafter referred to as OK1993 model) given by Ogata and Katsura (1993), which



89 has the advantage of simultaneously determining the minimum magnitude of completeness and obtaining  
90  $b$  values. In this paper, we will use this approach to study the spatiotemporal heterogeneity of  $b$  values  
91 for the 2019 Changning  $M_S$  6.0 earthquake.

92 The OK1993 model uses the seismic detection rate function  $q(M)$  to describe the complete detection  
93 degree of earthquake events with different magnitudes in the magnitude-frequency distribution:

$$94 \quad q(M|\mu, \sigma) = \frac{1}{\sqrt{2\pi\sigma^2}} \int_{-\infty}^M e^{-\frac{(x-\mu)^2}{2\sigma^2}} dx \quad (1)$$

95 where  $M$  is the magnitude, the parameter  $\mu$  represents the corresponding magnitude to the detection rate  
96 of 50%, and  $\sigma$  indicates the corresponding magnitude range. The actual earthquake probability density  
97 function and the log-likelihood function of the OK1993 model can be expressed as:

$$98 \quad P(M|\beta, \mu, \sigma) = \frac{e^{-\beta M} q(M|\mu, \sigma)}{\int_{-\infty}^{+\infty} e^{-\beta M} q(M|\mu, \sigma) dM} = \beta e^{-\beta(M-\mu)+\beta^2\sigma^2/2} q(M|\mu, \sigma) \quad (2)$$

$$99 \quad \ln L(\theta) = n \ln \beta - \sum_{i=1}^n [\beta M_i - \ln q(M_i|\mu, \sigma)] + n\beta\mu - \frac{n}{2}\beta^2\sigma^2 \quad (3)$$

100 The  $\{M_1, M_2, \dots, M_n\}$  in the above formula is the magnitude of a given series of observational events and  
101 the power exponent  $\beta = b \ln 10$ . The parameter  $[\beta, \mu, \sigma]$  can be obtained by fitting the above formula  
102 using the maximum likelihood method. The Bayesian information criterion  $BIC = -\ln L(\theta) +$   
103  $k/2 \ln(n)$  be adopted to calculate the corresponding BIC value and select the optimal models. Since  
104 each grid node is composed of spatial coordinates  $[x, y]$  and three parameters  $[\beta, \mu, \sigma]$  in the OK1993  
105 model, so the total number of freedom degrees is  $k = 5 \times \text{num of node}$  in the entire study region.

106 The construction of the data-driven approach can be achieved by the Voronoi tessellation with limited  
107 boundaries. Voronoi tessellation refer to a unique set of continuous polygon partitioning schemes  $\{P_i, i$   
108  $= 1, 2, \dots, n\}$  given by a set of spatial nodes  $S = \{s_1, s_2, \dots, s_n\}$  in two-dimensional or three-dimensional  
109 space. The polygon  $P_i = \{x \mid \text{dist}(x, s_i) \leq \text{dist}(x, s_j), i \neq j\}$ , where  $\text{dist}(a, b)$  denotes the Euclidean distance  
110 between two points. Voronoi tessellation also benefits from the uniqueness of its spatial division, so it is  
111 widely used in computing science, political elections, and many other studies (Rubner et al., 2000; Svec  
112 et al., 2007). The calculation steps of the data-driven approach include: (1) randomly throwing a certain  
113 number of nodes in the study area and performing Voronoi meshing, with the number of grid nodes  
114 gradually increasing from 2 to 40. To ensure that the Voronoi tessellation covers the possibility of various  
115 spatial region segmentation, each number of grid nodes is randomly thrown 100 times. (2) Calculate  
116 OK1993 model parameters and BIC values for  $(2 + 3 + \dots + 40) \times 100 = 81900$  Voronoi cells obtained from  
117 3900 tessellations (or spatial calculation models). Sum the BIC values of all the Voronoi cells obtained



118 from each tessellation and use it as the basis for judging whether this spatial calculation model is the  
119 optimal model; (3) Among the 3900 spatial calculation models, 100 models (marked as best-100) with  
120 smaller BIC values were selected as the optimal models, and the parameters  $[\beta, \mu, \sigma]$  of the ensemble  
121 median ( $Q_2$ ) and median absolute deviation (MAD) were used as the final calculation results. The  $b$  value  
122 can be obtained by  $b = \beta / \ln 10$ .

123 The maximum likelihood calculation of the OK1993 model parameter is not performed for the number  
124 of earthquakes  $N_1 < 5$  contained in a Voronoi cell, so the actual number of effective cells  $N_v$  obtained by  
125 each tessellation is used, to distinguish the number of randomly thrown nodes. Although the value of  $N_1$   
126 may affect the parameter fitting error in some polygons with a small number of events, considering that  
127 the OK1993 model in the form of continuous distribution function has the advantage of obvious fit  
128 adaptability compared to the traditional linear Frequency-Magnitude Distribution (FMD) function in a  
129 small number of data cases, this setting also ensures that the spatial division can obtain more polygon  
130 calculation results, and the final result of the parameters is expressed by the ensemble median value, so  
131 the effect of this method of value-taking on the final result is minimal.

132 In the above calculation steps, the setting of the maximum number of nodes, the number of random  
133 throws, etc. has obvious subjectivity. However, due to the fact that the data-driven approach actually  
134 obtains a very stable final result when the number of divisions and the number of grid nodes are sufficient  
135 (Si and Jiang, 2019), for example, when the maximum number of nodes is 100, each type of nodes are  
136 randomly thrown 1000 times, and the final result obtained when 1000 optimal models are selected is  
137 almost the same as the result of this paper.

### 138 **Study Region and Data Used**

139 The 2019 Changning  $M_S$  6.0 earthquake sequence occurred in the basin-mountain junction in the southern  
140 margin of the Sichuan Basin, where the tectonic activity is relatively weak. The seismicity in the area is  
141 mainly controlled by folds and associated faults. The intensity of historically destructive earthquakes is  
142 low in the area where aftershocks extend. No earthquake with magnitude above 5.0 has been recorded in  
143 this area before the Changning  $M_S$  6.0 earthquake. According to Yi et al. (2019), it is inferred that the  
144 occurrence of the Changning  $M_S$  6.0 earthquake sequence may be related to the Baixiangyan-Shizitan  
145 anticline and the Shuanghechang anticline and their associated fault activities. Figure 1 shows the study  
146 area of this paper. We will focus on the rectangular area A'B'C'D' where the aftershock sequence mainly



147 occurred and the rectangular area ABCD where the surrounding earthquakes are active.

148 We used earthquake catalogs and bulletins provided by the Sichuan Regional Seismic Network from  
149 2009/01/01 to 2019/07/17. To obtain relatively reliable parameters such as the epicenter location and  
150 focal depth, the double-difference algorithm HypoDD (Waldhauser and Ellsworth, 2000) was used to  
151 relocate the earthquakes. Among the data we used, a total of 21246 seismic events that meet the  
152 requirements of the HypoDD method are not less than 4 arrivals, including 516649 P-wave arrivals,  
153 506809 S-wave arrivals, and 59 permanent seismic stations and temporary seismic stations are used  
154 which are located in Sichuan and surrounding provinces. We used a 12-layer one-dimensional crustal  
155 velocity model (Xie et al., 2012) during the relocation. The ratio of  $V_P$  to  $V_S$  is set to 1.730.

156 A total of 18371 earthquake events were relocated (Fig. 1), of which the smallest event had a magnitude  
157 of -1.0. Among them, there were 13728 and 4642 earthquakes before and after the  $M_S$  6.0 mainshock,  
158 respectively. The horizontal and vertical uncertainties are 0.425 km, 0.457 km and 0.654 km, respectively.

159 The average root mean square (RMS) of the travel-time residuals was reduced to 0.162 s. There were  
160 2875 events were discarded, which accounted for 13.53% of original catalogue. Most of their magnitudes  
161 range between  $M_L$  0.3 to  $M_L$  1.4 (corresponding to the intervals of cumulative number 10% ~ 90%).  
162 Considering that the data-driven approach used in this paper is the selection and ensemble averaging of  
163 a large number of random space partitioning schemes, and that the OK1993 model is a continuous  
164 function of the magnitude-frequency distribution, the effect of these excluded events on the calculation  
165 result of  $b$  value can be ignored.

166 As can be seen from the spatial distribution of the relocated earthquakes shown in Figure 1, the  
167 aftershocks are mainly distributed in the northwest direction of the mainshock epicenter and extend along  
168 the Changning anticline with a length about 27 km, which is much longer than the rupture scale of about  
169 10 km for a  $M$  6 earthquake accordance with the empirical formula given by Well and Coppersmith  
170 (1994). Besides, the shape of the aftershock distribution is not simply linear; there are obvious inflections  
171 in the middle segment, and in the northwest there is a branch approximately perpendicular to the direction  
172 of aftershock distribution. There are relatively few aftershocks near the epicenter of the mainshock, and  
173 a large number of aftershocks occurred in the northwest.

174 In the aftershock sequence of the Changning  $M_S$  6.0 earthquake, there are 4 aftershocks with magnitudes  
175 exceeding  $M_S$  5.0, which are 2019/06/17  $M_S$  5.1, 2019/06/18  $M_S$  5.3, 2019/06/22  $M_S$  5.4, and 2019/07/04  
176  $M_S$  5.6 earthquake, respectively.



177

178

Fig. 1

179 To facilitate the calculation of  $b$  values and the display of the results, we have selected only the events  
180 within the rectangular area A'B'C'D' where almost all aftershocks are concentrated and the rectangular  
181 area ABCD where a large number of earthquakes existed before the mainshock occurred. The positions  
182 of these earthquakes were transformed by Cartesian coordinates and rotated according to the origin point  
183 (104.986°E, 28.395°N) of the coordinates so that the aftershock sequence can be spread horizontally in  
184 the new coordinate system. The epicenter distribution after coordinate transformation is shown in Figure  
185 2a-c show the spatiotemporal distribution on the distance versus rank of index 2-D map of the earthquake  
186 within the rectangular frame A'B'C'D'.

187

188

Fig. 2

### 189 **Spatial Distribution of $b$ values on Surface and Depth Profiles**

190 According to the technical process of the data-driven approach described above, after Voronoi  
191 tessellation, calculation of the BIC values, and selection of the optimal models, the ensemble median ( $Q_2$ )  
192 and ensemble median absolute deviation (MAD) of  $b$  values can be obtained. Figure 3 shows an example  
193 of calculating the parameters of the OK1993 model in terms of the frequency-magnitude distribution  
194 based on a data-driven approach. Figure 3a is the distribution of those BIC values corresponding to the  
195 number of effective cells  $N_V$ , and the red dots are the selected best-100 models. Figure 3b shows an  
196 example in the best-100 models, that is, in the case of  $N_V = 20$ , the Voronoi tessellation in the rectangular  
197 study area ABCD and the distribution of  $b$  values obtained by its calculation. Figure 3c shows an example  
198 of the fitting result of the Ogata-Katsura 1993 model corresponding to a cell in Figure 3b. The OK1993  
199 model parameters obtained by the fitting are  $b = 0.714$ ,  $\mu = 0.376$  and  $\sigma = 0.247$ .

200

201

Fig. 3

202 We calculated the distribution of the ensemble median  $b$  value in the rectangular region ABCD and the  
203 depth profile of the rectangular region A'B'C'D', respectively. The results are shown in Figure 4. Figures



204 4a-b are the results before the Changning  $M_S6.0$  earthquake and the entire study period, respectively. The  
205 results show that the  $b$  values exhibit a strong heterogeneous spatial distribution in the rectangular region  
206 ABCD before the Changning  $M_S6.0$  earthquake. Low  $b$  values are mainly distributed in the eastern half  
207 of the area, with its lowest value being  $b = 0.732$  and located near the epicenter of the mainshock. Low  
208  $b$  value contours are mainly distributed in the NE-SW direction and are consistent with the direction of  
209 Shuanghechang anticline and their associated faults passing through the main epicenter. In the western  
210 part of the rectangular region ABCD, where high  $b$  values are distributed, with a largest value of  $b =$   
211 2.200. This indicates that before the Changning  $M_S 6.0$  earthquake, the differential stress near the  
212 epicenter of the mainshock was high, but the spatial scale of this larger differential stress was much  
213 smaller than the scale of the aftershock spatial distribution. The spatial distribution of  $b$  values calculated  
214 using all seismic events (see Fig. 4b) shows that the area with low  $b$  values in the region ABCD is  
215 significantly enlarged, and the  $b$  values in the rectangular region A'B'C'D' are almost less than 1.0 and  
216 further reduced to 0.698 near the epicenter of the mainshock. This phenomenon of a significant decrease  
217 in  $b$  value of the aftershock sequence after the mainshock widely exists in many earthquake cases (El-  
218 Isaa and Eatonb, 2014; Gulia and Wiemer, 2019).

219 Figures 4c-d show the distribution of ensemble median  $b$  value on the depth profile of the rectangular  
220 area A'B'C'D', and correspond to the results before the Changning  $M_S6.0$  earthquake and all study periods,  
221 respectively. The calculation results after considering the depth information of the earthquake show that  
222  $b$  values also have strong heterogeneity at different depths. Among them, in Figure 4c, low  $b$  values are  
223 mainly distributed at depth of 4 ~ 15 km and contains the source of the Changning  $M_S 6.0$  earthquake  
224 and the 2019/06/17  $M_S 5.1$  earthquake. The lowest  $b$  value is about 0.493, which is much smaller than  
225 the minimum value in Figure 4a. In Figure 4d, considering the occurrence of the Changning  $M_S6.0$   
226 earthquake sequence, the distribution area of low  $b$  values expands in the NW direction, and the lowest  
227  $b$  value is about 0.501, which is close to that in Figure 4c. Compared with the results obtained by ignoring  
228 the depth information of the earthquake in Figure 4a-b, the results obtained by Figure 4c-d reveal more  
229 significant heterogeneity of  $b$  values. When investigating this problem to the depth of the crust. Lower  $b$   
230 values may indicate that there should be greater differential stress at the depth where the source area of  
231 the mainshock is located, and it is easily ignored by  $b$  value calculations that usually do not consider the  
232 depth information of earthquake events.



233

234

Fig. 4

235 Figure 5 shows the spatial distribution of the median absolute deviation (MAD) of  $b$  values by the data-  
236 driven approach according to Figure 4. The ensemble MAD  $b$  value is smaller in the most region of  
237 Figure 5a-d, especially in the rectangular region A'B'C'D', which implies that these regions have  
238 relatively stable distribution and reliable ensemble median  $b$  values.

239

240

Fig. 5

#### 241 **Spatiotemporal Heterogeneity of $b$ values**

242 Considering that  $b$  value usually changes over time before and after a strong earthquake, this paper not  
243 only examines the spatial distribution of  $b$  values in the surface and depth profiles but also discusses the  
244 spatiotemporal distribution of  $b$  values for earthquake events in the rectangular area A'B'C'D' where the  
245 Changning  $M_S 6.0$  sequence is located. Due to the strong temporal and spatial inhomogeneity of seismic  
246 activity, especially clustering in time, this brings great difficulties to obtaining a stable and reliable  $b$   
247 value and clearly showing the temporal and spatial variation of the  $b$  value. In order to reduce this  
248 difficulty to a certain extent, here we use the index of earthquake occurrence instead of time, that is, the  
249 earthquake is projected on a pseudo-time axis of the index number of the occurrence time sequence.  
250 Using the same calculation method as in Figure 4 and Figure 5, the distributions of ensemble median  $b$   
251 values and ensemble MAD  $b$  values on the distance-index map are obtained. The corresponding results  
252 are shown in Figure 6 and Figure 7. Considering the possible abrupt change of the regional stress field  
253 due to strong earthquakes such as the Changning  $M_S 6.0$  earthquake, in the study of the spatiotemporal  
254 distribution of  $b$  values, we follow two schemes: study the entire period as a whole, and the two periods  
255 before and after the Changning  $M_S 6.0$  earthquake were studied separately. The calculation results under  
256 the two schemes are shown in Figure 6a-b, respectively.

257

258

Fig. 6

259 It can be seen in Figure 6a that before the Changning  $M_S 6.0$  earthquake occurred, in the segment between



260 -5 km and -10 km near the A'/B' end and a length of about 10 km (NW direction of the aftershocks in  
261 Fig. 1), showed relatively stable high  $b$  values, with the maximum value exceeding 2.0. In the segment  
262 between -5 km and 12 km near the C'/D' end and a length of about 17 km (the SE direction of the  
263 aftershocks in Figure 1, including the nucleation point of the mainshock), showed relatively stable low  
264 values before the Changning  $M_s$  6.0 earthquake occurred, and the range of the low  $b$  values gradually  
265 narrowed down and concentrated towards the nucleation point of the mainshock. After the Changning  
266  $M_s$  6.0 earthquake occurred, the  $b$  values in the entire spatial range from A'/B' to C'/D' decreased  
267 significantly. Among them, the  $b$  values in the 0 km ~ 12 km segment where the nucleation point of the  
268 mainshock is located have recovered rapidly, while the  $b$  values in the 0 km ~ -15 km segment have  
269 increased at a slower rate.

270 From the results before and after the Changning  $M_s$  6.0 earthquake shown in Figure 6b, it can be seen  
271 that the occurrence of the mainshock has a greater impact on the continuity of time variant  $b$  values. This  
272 means that the spatiotemporal evolution image of the  $b$  values given in Figure 6a over the entire study  
273 period is not physically valid. Correspondingly, the decrease of pre-mainshock  $b$  values and the sudden  
274 expansion of the low  $b$  values may be a kind of artifact caused by the subsequent aftershocks brought  
275 into the calculation (Lei et al., 2019).

276 Compared with Figure 6a, the results in Figure 6b show that before the Changning  $M_s$  6.0 earthquake,  
277 the shortening and concentration changes for the low  $b$  value segment near the C'/D' end, and the  
278 expansion process of the high  $b$  value segment on the near the A'/B' end is performed simultaneously.  
279 This implies that a significantly higher differential stress area is concentrated toward the nucleation point  
280 of the mainshock. Figure 7 a-b show the distribution of ensemble MAD  $b$  values according to Figure 6  
281 a-b, where higher ensemble MAD  $b$  values mainly appear in some areas with higher  $b$  values in Figure  
282 6 a-b.

283

284

Fig. 7

## 285 Discussion

286 In the pattern of  $b$  value spatial heterogeneity before strong earthquakes, the locations of rupture  
287 nucleation points, sliding distributions, and aftershock distributions of some strong earthquakes were



288 observed to correspond to areas with lower  $b$  values, such as the Parkfield  $M = 6.0$  earthquake on  
289 September 28, 2004 (Wiemer and Wyss, 1997; Schorlemmer et al., 2004; Schorlemmer and Wiemer,  
290 2005). However, the significant spatial heterogeneity of  $b$  values obtained from the studies of these  
291 earthquakes is suspected to be related to the subjective arbitrariness of the calculation rules (Kamer and  
292 Hiemer, 2015). The calculation results based on the data-driven method (Si and Jiang, 2019) in this paper  
293 show that significant spatial heterogeneity of  $b$  values can still be observed before the Changning  $M_s 6.0$   
294 earthquake, especially on the depth profile of the fault. Moreover, according to the empirical relationship  
295 between the magnitude and rupture scale of Wells and Coppersmith (1994), the low-value spatial scale  
296 of  $b < 0.75$  in Figure 4c is also close to the rupture length of about 10 km for the M 6.0 mainshock. This  
297 also means that it is still feasible to use the spatial heterogeneity of the  $b$  values to identify the locked  
298 asperities and determine the location of future strong earthquakes if more cases are verified.

299 There is still much controversy over the time variation pattern of  $b$  values in the source area before a  
300 strong earthquake. Although the  $b$  values to drop prior to failure was found in laboratory fracturing  
301 experiments on relatively complete rock samples (e.g., Thompson et al., 2006; Lei, 2019), and the case  
302 study of strong earthquakes (Nanjo et al., 2012; Schurr et al., 2014; Bayrak et al., 2017; Huang et al.,  
303 2020), but a large number of reported  $b$  values time variation before actual strong earthquakes are still  
304 considered to have no statistically significant predictive power (Parsons, 2007), or some studies have  
305 found that the temporal variation of  $b$  values corresponding to asperities are synchronized with loading  
306 rate and shear stress (Tormann et al., 2013). Schorlemmer et al. (2004) and Wiemer and Wyss (2002)  
307 studied some earthquake cases and concluded that the  $b$  value is quite stable over time and it is difficult  
308 to observe a significant change. The study of the relationship between acoustic emission events and stress  
309 in the stick-slip experiment shows that the complexity of the time variation of  $b$  values observed when  
310 sliding on rough fault planes may be due to fault-structure heterogeneity (Goebel et al., 2013). In this  
311 study of the Changning  $M_s 6.0$  earthquake, we did not simply examine the time variation of the  $b$  value  
312 in a fixed spatial range, but calculated the pattern migration of the  $b$  value in a 2-D spatiotemporal space.  
313 We found that as the time approaches the occurrence of the mainshock, the spatial range of the low  $b$   
314 values gradually shrinks and focuses on the vicinity of the rupture nucleation point, and the  $b$  values does  
315 not decrease significantly. Under the assumption that the fault-structural heterogeneity will not change  
316 in the short term, this pattern migration may reflect that the high differential stress area where the  
317 nucleation point is located is eroded by the surrounding area (high  $b$  value) that increases the pore fluid



318 pressure.

319 For the spatiotemporal heterogeneity of the  $b$  value of the aftershocks of the 2019 Changning  $M_s$  6.0  
320 earthquake, we noticed that the aftershocks expanded spatially to areas with high pre-mainshock  $b$  values  
321 in the northwest direction, and the length of the aftershock area was significantly longer than the rupture  
322 scale of the earthquake (see Fig. 6b). Since the aftershocks do not exhibit relatively slow spatiotemporal  
323 migration behavior, the physical mechanism that drives the aftershocks of this earthquake cannot be  
324 explained by either the traditional stress corrosion model (Das and Scholz, 1981), or by frictional afterslip  
325 model (Perfettini et al., 2018; Koper et al., 2018). Some views suggest that aftershock activity in high  $b$   
326 value regions may be related to the reactivation of highly fractured fault zones, the redistribution of stress  
327 fields, and the role of fluids trapped in microfractures (Aktar et al., 2004). Long et al. (2020) imaging the  
328 velocity structure of the area where the Changning  $M_s$  6.0 earthquake was located, showing that there is  
329 an obvious S-wave low-velocity anomaly at the depth of 3 to 8 km in the northwestern segment of the  
330 aftershock. In this paper, this S-wave low-velocity anomaly region also corresponds to the distribution  
331 of high  $b$  values, which may be related to the fluid intrusion or high pore pressure. Therefore, we believe  
332 that the abundant aftershocks produced by this mainshock, and the active area that exceeds the rupture  
333 scale of the mainshock are more likely to be caused by the mainshock triggering a series of complex  
334 structural earthquakes northwest of the nucleation point. The dynamic expansion of the high pre-  
335 mainshock  $b$  value region to the nucleation point also creates conditions for the triggering of a large  
336 number of aftershocks and the widespread spatially.

337 In addition, the  $b$  values of the aftershocks first dropped rapidly to about 0.5, then gradually recovered,  
338 and returned to the pre-seismic level after the fourth magnitude 5 strong aftershock (excluding high  $b$   
339 value areas). The phenomenon that the  $b$  values of the aftershock sequence decreases immediately after  
340 the mainshock to a rapid recovery has been observed in many earthquake cases (El-Isaa and Eatonb,  
341 2014; Tormann et al., 2015). Unlike most aftershock sequences, where the  $b$  value generally increases  
342 by 20% after the mainshock, this sudden decrease in  $b$  value is considered to be related to the occurrence  
343 of subsequent strong aftershocks or larger earthquakes (Gulia and Wiemer, 2019). In the aftershock  
344 sequence of the Changning  $M_s$  6.0 earthquake, the rapidly decreasing  $b$  value of the aftershocks was  
345 accompanied by 4 strong aftershocks with magnitudes greater than 5.0, which is consistent with the  
346 phenomenon revealed by previous people. This may also support the idea of discrimination between  
347 foreshocks and aftershocks by real-time monitoring of the  $b$  value in aftershock sequences.



348 **Conclusions**

349 To reveal whether there is spatiotemporal heterogeneity of  $b$  values before and after the 2019 Changning  
350  $M_S$  6.0 earthquake, and to overcome the subjectivity of the choice of data used for calculation, we applied  
351 a parameter calculation method for the OK1993 model of magnitude-frequency distribution according to  
352 the data-driven idea to calculate  $b$  values. We also investigated the distribution characteristics of  $b$  values  
353 from three different ways: horizontal surface distribution, depth profile distribution, and in the distance-  
354 rank of index map. The main conclusions are as follows:

355 1. The  $b$  values before and after the Changning  $M_S$  6.0 earthquake showed strong spatiotemporal  
356 heterogeneity on the horizontal surface distribution, depth profile distribution, and distance-rank of index  
357 map. Among them, before the Changning  $M_S$  6.0 earthquake, there were obvious low  $b$  value distributions  
358 near the epicenter of the mainshock and within the depth range of 3 to 12 km. The correlation shows that  
359 there may be significantly higher differential stress in the source area before the Changning  $M_S$  6.0  
360 earthquake. The northwestern segment of the aftershocks has a distinctly high  $b$  value distribution, which  
361 coincides with the S-wave low-velocity anomaly region shown by the velocity structure imaging.

362 2. The  $b$  value spatiotemporal distribution results show that before the Changning  $M_S$  6.0 earthquake, the  
363 high  $b$  value region of the NW segment spread by aftershocks gradually expanded and approached the  
364 nucleation point as the time approached the failure time of mainshock. This may be related to the fluid  
365 intrusion or increased pore pressure in the rock. A large number of aftershocks were produced and the  
366 area where the aftershocks were spread was significantly larger than the rupture scale of the mainshock.  
367 It may be that the mainshock triggered seismicity in the NW direction where the fluid intrudes or pore  
368 pressure increased.

369 3. The  $b$  values of the aftershocks of the Changning  $M_S$  6.0 earthquake decreased rapidly and gradually  
370 recovered after the mainshock, indicating a higher differential stress level in the aftershock area. The  
371 time variation of low  $b$  value is synchronized with the occurrence of strong aftershocks with  $M \geq 5.0$ ,  
372 showing the application potential that can be used to distinguish between foreshocks and aftershocks.

373 4. Although the distribution characteristics of  $b$  values before and after the Changning  $M_S$  6.0 earthquake  
374 were qualitatively consistent when they were studied in different space-time dimensions, there were  
375 significant differences in specific  $b$  value. For example, the minimum  $b$  value of the Changning  $M_S$  6.0  
376 earthquake on the depth profile distribution is about 0.493, but it is about 0.732 when the seismic depth



377 information is ignored and only calculated on the surface. This inconsistency needs special attention  
378 when studying the spatiotemporal heterogeneity of  $b$  values.

### 379 **Acknowledgment**

380 This study is supported by the program of China Seismic Experimental Site (CSES, No. 2019CSES0106,  
381 the program of basic resources investigation of science and technology (No. 2018FY100504). The  
382 earthquake catalog used in this paper was provided by the Sichuan Earthquake Agency. The Multi-  
383 Parametric Toolbox 3.0 (<https://www.mpt3.org/Main/HomePage>, last accessed June 2018) is used for the  
384 analysis of parametric optimization and computational geometry.

### 385 **References**

386 Aktar, M., S. Özalaybey, M. Ergin, H. Karabulut, M.-P. Bouin, C. Tapırdamaz, F. Bıçmen, A. Yörük  
387 and M. Bouchon (2004). "Spatial variation of aftershock activity across the rupture zone of the 17  
388 August 1999 Izmit earthquake, Turkey." Tectonophysics **391**(1-4): 325-334.

389 Amelung, F. and G. King (1997). "Earthquake scaling laws for creeping and non-creeping faults."  
390 Geophysical Research Letters **24**(5): 507-510.

391 Amorèse, D., J.-R. Grasso and P. Rydelek (2010). "On varying  $b$ -values with depth: results from  
392 computer-intensive tests for Southern California." Geophysical Journal International **180**(1): 347-  
393 360.

394 Bayrak, E., S. Yılmaz and Y. Bayrak (2017). "Temporal and spatial variations of Gutenberg-Richter  
395 parameter and fractal dimension in Western Anatolia, Turkey." Journal of Asian Earth Sciences,  
396 **138**: 1-11.

397 Das, S. and C. Scholz (1981). "Theory of time-dependent rupture in the Earth." Journal of  
398 Geophysical Research: Solid Earth **86**(B7): 6039-6051.

399 Del Pezzo, E., F. Bianco and G. Saccorotti (2003). "Duration magnitude uncertainty due to seismic  
400 noise: Inferences on the temporal pattern of GR  $b$ -value at Mt. Vesuvius, Italy." Bulletin of the  
401 Seismological Society of America **93**(4): 1847-1853.



- 402 El-Isaa, Z. H. and D. W. Eaton (2014). "Spatiotemporal variations in the b-value of earthquake  
403 magnitude–frequency distributions: Classification and causes." Tectonophysics **615–616**: 1-11.
- 404 Goebel, T. H. W., D. Schorlemmer, T. Becker, G. Dresen and C. Sammis (2013). "Acoustic  
405 emissions document stress changes over many seismic cycles in stick-slip experiments."  
406 Geophysical Research Letters **40**(10): 2049-2054.
- 407 Gulia, L. and S. Wiemer (2019). "Real-time discrimination of earthquake foreshocks and  
408 aftershocks." Nature **574**(7777): 193-199.
- 409 Gulia, L., S. Wiemer and D. Schorlemmer (2010). "Asperity-based earthquake likelihood models  
410 for Italy." Annals of Geophysics **53**(3): 63-75.
- 411 Hainzl, S. and T. Fischer (2002). "Indications for a successively triggered rupture growth underlying  
412 the 2000 earthquake swarm in Vogtland/NW Bohemia." Journal of Geophysical Research: Solid  
413 Earth **107**(B12): ESE 5-1-ESE 5-9.
- 414 Huang, H., L. S. Meng, R. Bürgmann, W. Wang and K. Wang (2020), "Spatio-temporal foreshock  
415 evolution of the 2019 M 6.4 and M 7.1 Ridgecrest, California earthquakes." Earth and Planetary  
416 Science Letters, **551**: 116582.
- 417 Hutton, K., J. Woessner and E. Hauksson (2010). "Earthquake monitoring in southern California  
418 for seventy-seven years (1932–2008)." Bulletin of the Seismological Society of America **100**(2):  
419 423-446.
- 420 Kagan, Y. Y. (1999). "Universality of the seismic moment-frequency relation." Pure and Applied  
421 Geophysics **155**(2): 537-573.
- 422 Kamer, Y. and S. Hiemer (2015). "Data-driven spatial *b* value estimation with applications to  
423 California seismicity: To *b* or not to *b*." Journal of Geophysical Research: Solid Earth **120**(7): 5191-  
424 5214.
- 425 Koper, K. D., K. L. Pankow, J. C. Pechmann, J. M. Hale, R. Burlacu, W. L. Yeck, H. M. Benz, R.  
426 B. Herrmann, D. T. Trugman and P. M. Shearer (2018). "Afterslip enhanced aftershock activity  
427 during the 2017 earthquake sequence near Sulphur Peak, Idaho." Geophysical Research Letters  
428 **45**(11): 5352-5361.



- 429 Lei, X. L. (2019). "Evolution of  $b$ -value and fractal dimension of acoustic emission events during  
430 shear rupture of an immature fault in Granite." Applied Sciences **9**(12): 2498.
- 431 Lei, X. L. and T. Satoh (2007). "Indicators of critical point behavior prior to rock failure inferred  
432 from pre-failure damage." Tectonophysics **431**(1-4): 97-111.
- 433 Lei, X., Z. Wang and J. Su (2019). "Possible link between long-term and short-term water injections  
434 and earthquakes in salt mine and shale gas site in Changning, south Sichuan Basin, China." Earth  
435 and Planetary Physics **3**(6): 510-525.
- 436 Long, F., Z. Zhang, Y. Qi, M. Liang, X. Ruan, W. Wu, G. Jiang and L. Zhou (2020). "Three  
437 dimensional velocity structure and accurate earthquake location in Changning–Gongxian area of  
438 southeast Sichuan." Earth and Planetary Physics **4**(2): 1-15.
- 439 Mori, J. and R. E. Abercrombie (1997). "Depth dependence of earthquake frequency-magnitude  
440 distributions in California: Implications for rupture initiation." Journal of Geophysical Research:  
441 Solid Earth **102**(B7): 15081-15090.
- 442 Murru, M., R. Console, G. Falcone, C. Montuori and T. SgROI (2007). "Spatial mapping of the  $b$   
443 value at Mount Etna, Italy, using earthquake data recorded from 1999 to 2005." Journal of  
444 Geophysical Research: Solid Earth **112**: B12303.
- 445 Nandan, S., G. Ouillon, S. Wiemer and D. Sornette (2017). "Objective estimation of spatially  
446 variable parameters of epidemic type aftershock sequence model: Application to California." Journal of Geophysical Research: Solid Earth **122**(7): 5118-5143.
- 448 Nanjo, K. Z., N. Hirata, K. Obara and K. Kasahara (2012). "Decade - scale decrease in  $b$  value prior  
449 to the M9 - class 2011 Tohoku and 2004 Sumatra quakes." Geophysical Research Letters **39**:  
450 L20304.
- 451 Ogata, Y. (2011). "Significant improvements of the space-time ETAS model for forecasting of  
452 accurate baseline seismicity." Earth, Planets and Space **63**(3): 6.
- 453 Ogata, Y. and K. Katsura (1993). "Analysis of temporal and spatial heterogeneity of magnitude  
454 frequency distribution inferred from earthquake catalogues." Geophysical Journal International  
455 **113**(3): 727-738.



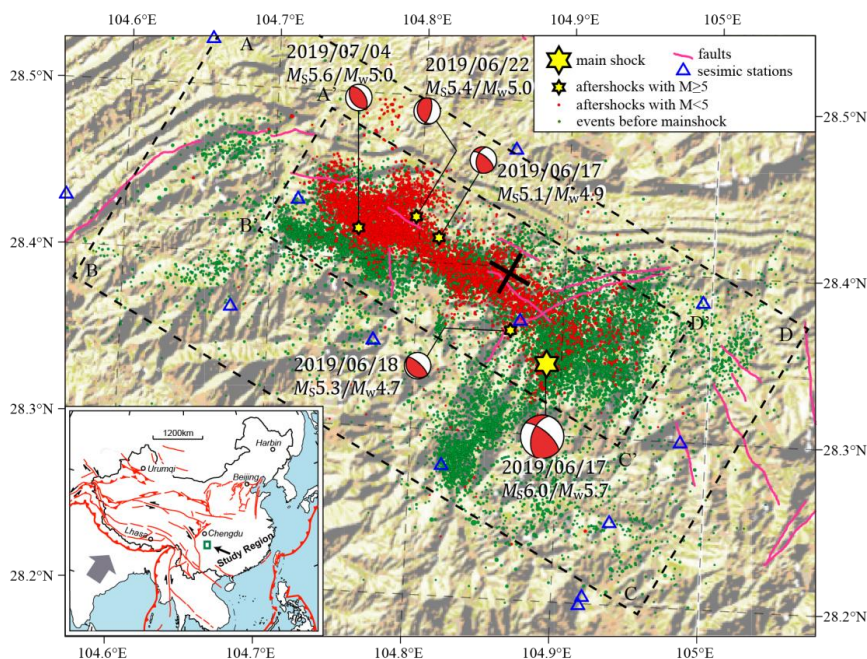
- 456 Parsons, T. (2007). "Forecast experiment: Do temporal and spatial *b* value variations along the  
457 Calaveras fault portend  $M \geq 4.0$  earthquakes?" Journal of Geophysical Research: Solid Earth  
458 **112**(B3): B03308.
- 459 Perfettini, H., W. Frank, D. Marsan and M. Bouchon (2018). "A model of aftershock migration  
460 driven by afterslip." Geophysical Research Letters **45**(5): 2283-2293.
- 461 Rubner, Y., C. Tomasi, L. J. Guibas (2000). "The earth mover's distance as a metric for image  
462 retrieval." International Journal of Computer Vision **40**: 99-121.
- 463 Sambridge, M., T. Bodin, K. Gallagher and H. Tkalčić (2013). "Transdimensional inference in the  
464 geosciences." Philosophical Transactions of the Royal Society A: Mathematical, Physical and  
465 Engineering Sciences **371**(1984): 20110547.
- 466 Scholz, C. H. (1968). "The frequency-magnitude relation of microfracturing in rock and its relation  
467 to earthquakes." Bulletin of the seismological society of America **58**(1): 399-415.
- 468 Schorlemmer, D. and S. Wiemer (2005). "Microseismicity data forecast rupture area." Nature  
469 **434**(7037): 1086-1086.
- 470 Schorlemmer, D., S. Wiemer and M. Wyss (2004). "Earthquake statistics at Parkfield: 1. Stationarity  
471 of *b* values." Journal of Geophysical Research: Solid Earth **109**(B12).
- 472 Schurr B, G. Asch, S. Hainzl, J. Bedford, A. Hoechner, M. Palo, R. Wang, M. Moreno, M. Bartsch,  
473 Y. Zhang, O. Oncken, F. Tilmann, T. Dahm, P. Victor, S. Barrientos and J. Vilotte (2014). "Gradual  
474 unlocking of plate boundary controlled initiation of the 2014 Iquique earthquake." Nature **512**: 299-  
475 302.
- 476 Si, Z. Y. and C. S. Jiang (2019). "Research on parameter calculation for the Ogata–Katsura 1993  
477 model in terms of the frequency–magnitude distribution based on a data-driven approach."  
478 Seismological Research Letters **90**(3): 1318-1329.
- 479 Stirling, M. W., S. G. Wesnousky and K. Shimazaki (1996). "Fault trace complexity, cumulative  
480 slip, and the shape of the magnitude-frequency distribution for strike-slip faults: A global survey."  
481 Geophysical Journal International **124**(3): 833-868.



- 482 Svec, L., S. Burden, A. Dilley (2007). "Applying Voronoi diagrams to the redistricting problem. "  
483 The UMAP Journal **28**: 313-32.
- 484 Thompson, B. D., R. P. Young and D. A. Lockner (2006). "Fracture in Westerly granite under AE  
485 feedback and constant strain rate loading: nucleation, quasi-static propagation, and the transition to  
486 unstable fracture propagation." Pure and Applied Geophysics **163**(5-6): 995-1019.
- 487 Toda, S., R. S. Stein, P. A. Reasenberg, J. H. Dieterich and A. Yoshida (1998). "Stress transferred  
488 by the 1995  $M_w=6.9$  Kobe, Japan, shock: Effect on aftershocks and future earthquake probabilities."  
489 Journal of Geophysical Research: Solid Earth **103**(B10): 24543-24565.
- 490 Tormann, T., B. Enescu, J. Woessner, and S. Wiemer (2015). "Randomness of megathrust  
491 earthquakes implied by rapid stress recovery after the Japan earthquake." Nature Geoscience **8**: 152-  
492 158.
- 493 Tormann, T., S. Wiemer, S. Metzger, A. Michael, and J. L. Hardebeck (2013). "Size distribution of  
494 Parkfield's microearthquakes reflects changes in surface creep rate." Geophysical Journal  
495 International **193**: 1474-1478.
- 496 Urbancic, T. I., C. I. Trifu, J. M. Long and R. P. Young (1992). "Space-time correlations of  $b$  values  
497 with stress release." Pure and Applied Geophysics **139**(3-4): 449-462.
- 498 Waldhauser, F. and W. L. Ellsworth (2000). "A double-difference earthquake location algorithm:  
499 method and application to the Northern Hayward fault, California." Bulletin of the Seismological  
500 Society of America **90**(6): 1353-1368.
- 501 Wells, D. L. and K. J. Coppersmith (1994). "New empirical relationships among magnitude, rupture  
502 length, rupture width, rupture area, and surface displacement." Bulletin of the seismological Society  
503 of America **84**(4): 974-1002.
- 504 Wiemer, S. and D. Schorlemmer (2007). "ALM: An asperity-based likelihood model for  
505 California." Seismological Research Letters **78**(1): 134-140.
- 506 Wiemer, S. and M. Wyss (1997). "Mapping the frequency-magnitude distribution in asperities: An  
507 improved technique to calculate recurrence times?" Journal of Geophysical Research: Solid Earth  
508 **102**(B7): 15115-15128.

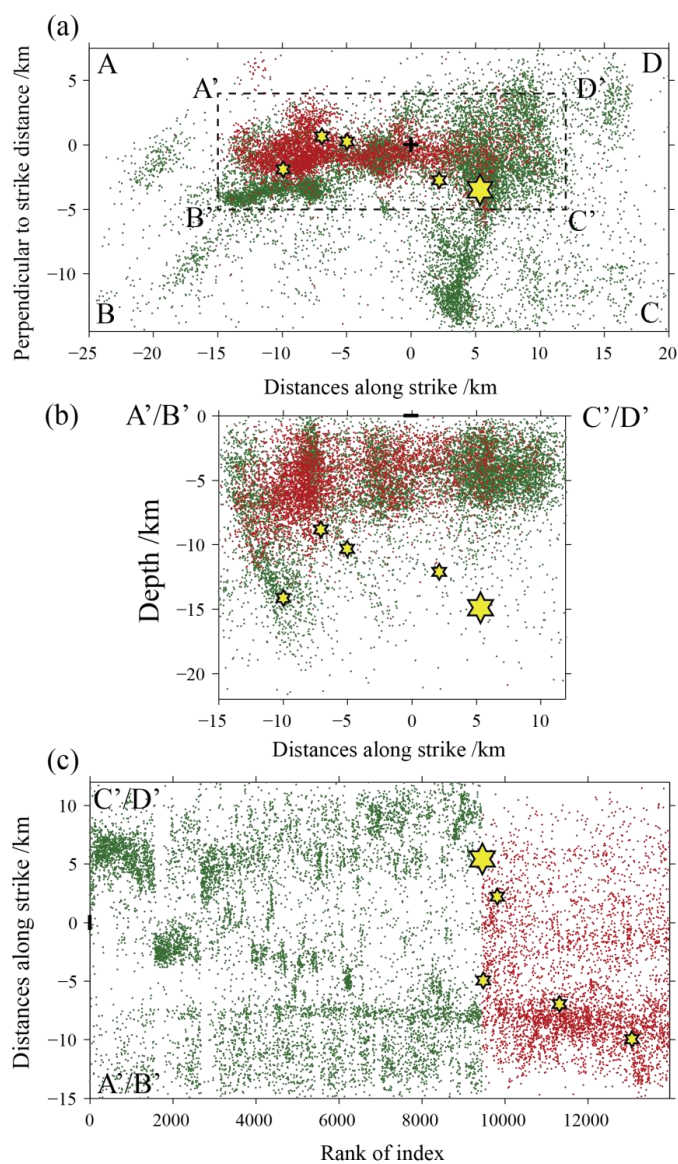


- 509 Wiemer, S. and M. Wyss (2002). Mapping spatial variability of the frequency-magnitude  
510 distribution of earthquakes. Advances in Geophysics **45**: 259-302.
- 511 Woessner, J. and S. Wiemer (2005). "Assessing the quality of earthquake catalogues: Estimating  
512 the magnitude of completeness and its uncertainty." Bulletin of the Seismological Society of  
513 America **95**(2): 684-698.
- 514 Wyss, M. (1973). "Towards a physical understanding of the earthquake frequency distribution."  
515 Geophysical Journal of the Royal Astronomical Society **31**(4): 341-359.
- 516 Wyss, M., D. Schorlemmer and S. Wiemer (2000). "Mapping asperities by minima of local  
517 recurrence time: San Jacinto-Elsinore fault zones." Journal of Geophysical Research: Solid Earth  
518 **105**(B4): 7829-7844.
- 519 Xie, J., S. Ni and X. Zeng (2012). "1 D shear wave velocity structure of the shallow upper crust in  
520 central Sichuan Basin." Earthquake Research in Sichuan (in Chinese) **143**(2): 20-24.
- 521 Yi, G. X., F. Long, M. J. Liang, M. Zhao, S. W. Wang, Y. Gong, H. Z. Qiao and J. R. Su (2019).  
522 "Focal mechanism solutions and seismogenic structure of the 17 June 2019  $M_s$  6.0 Sichuan  
523 Changning earthquake sequence." Chinese Journal of Geophysics (in Chinese) **62**(9): 3432-3447.
- 524  
525  
526  
527



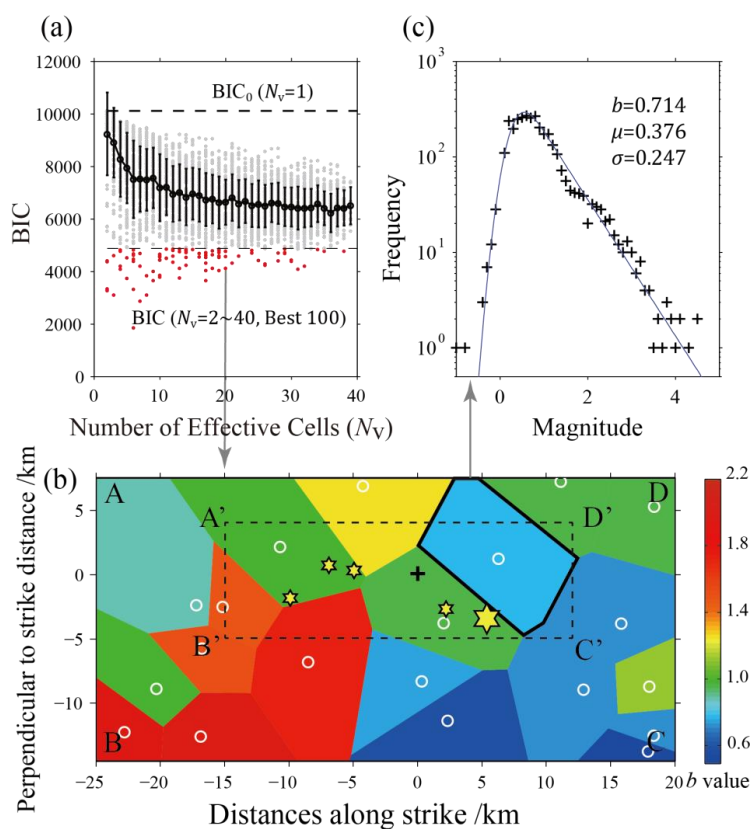
528

529 **Fig. 1** Distribution of seismicity in the Changning area. The red dots show the aftershocks of the Changning  
530  $M_s 6.0$  earthquake, and the green dots indicate the earthquakes that occurred before the Changning  
531  $M_s 6.0$  earthquake. Hexagonal stars mark the position of the mainshock and four aftershocks with  
532 magnitude no less than 5.0, and the corresponding focal mechanisms are marked. The dotted  
533 rectangular ABCD and A'B'C'D' show the two spatial regions for calculating the  $b$  value and rotating  
534 the coordinate system, and the cross symbol gives the origin where the coordinate system is rotated.  
535 The blue triangles show the location of seismic stations that record these earthquakes, and the solid  
536 pink lines represent active faults (He et al., 2019). The study region is shown in the location figure in  
537 the bottom-left by a green rectangle.

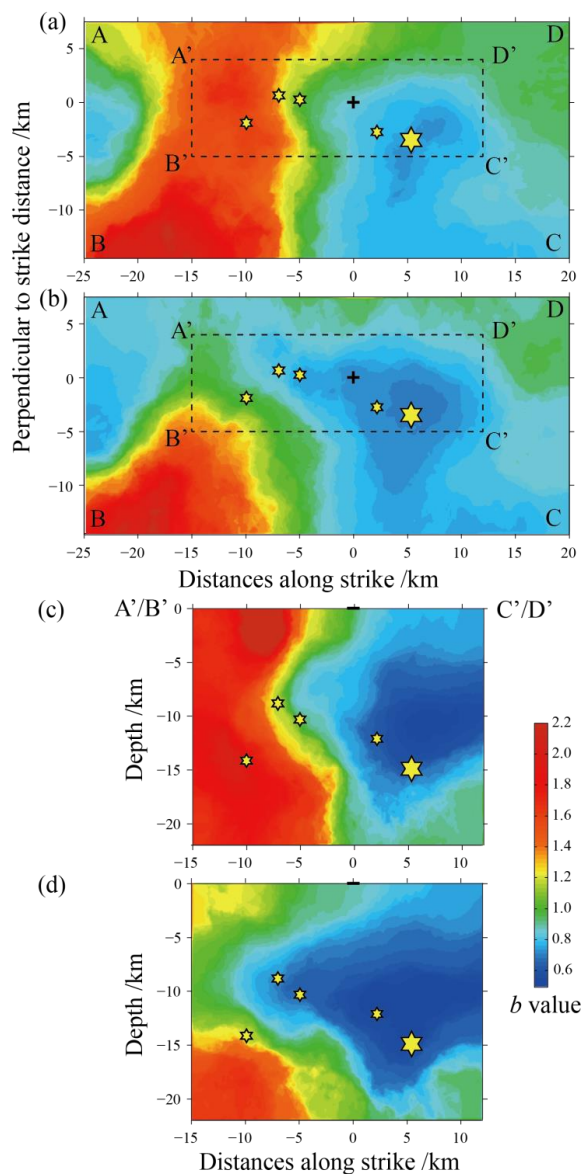


538

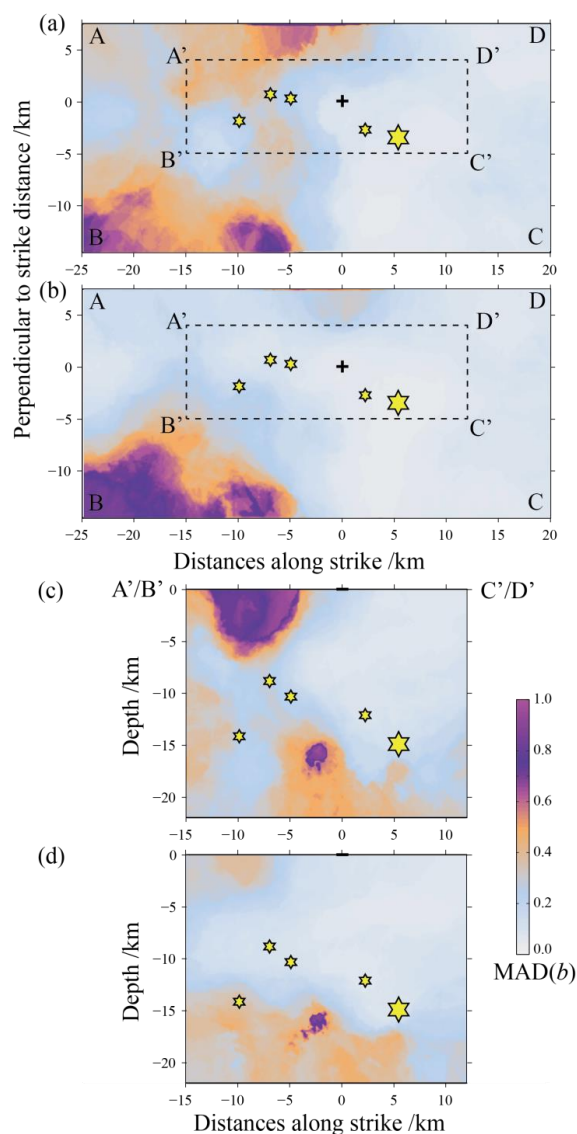
539 **Fig. 2** Distribution of seismicity for  $b$  values calculations. (a) Rotating the coordinate system to the seismic  
540 distribution along the direction of the aftershock distribution; (b) Projecting the earthquakes in the  
541 rectangular frame A'B'C'D' on the depth profile; (c) The temporal and spatial distribution on the  
542 distance versus rank of index 2-D map of the earthquakes within the rectangular frame A'B'C'D'. The  
543 meaning of the symbols is the same as in Fig. 1.



544  
 545 **Fig. 3** An example of calculating the parameters of the Ogata-Katsura 1993 model in terms of the frequency-  
 546 magnitude distribution based on a data-driven approach. (a) Distribution of BIC values versus the  
 547 number of effective cells  $N_v$  in the Voronoi tessellation. The black dots and error bars are  
 548 commensurate with the mean value and one standard deviation of BIC values under the corresponding  
 549  $N_v$ , respectively. The top horizontal dashed line marks the BIC values of the entire spatial region  
 550 without mesh generation ( $BIC_0, N_v=1$ ). The red dots show the BIC values with the best-100 solutions  
 551 are selected, while the gray dots are the other BIC results according to  $N_v$ . (b) Example of Voronoi  
 552 tessellation of  $N_v=20$  and one of the best-100 models selected. The white circles are the positions of the  
 553 Voronoi nodes, and the resulting partitions are color coded by their estimated  $b$  values (obtained from  
 554 the  $\beta$ -value in the Ogata-Katsura 1993 model). (c) Example of fitting result for the frequency-  
 555 magnitude distribution (FMD) of the Ogata-Katsura 1993 (OK1993) model in the Voronoi cell  
 556 indicated by a thick line in subgraph (b).  
 557  
 558



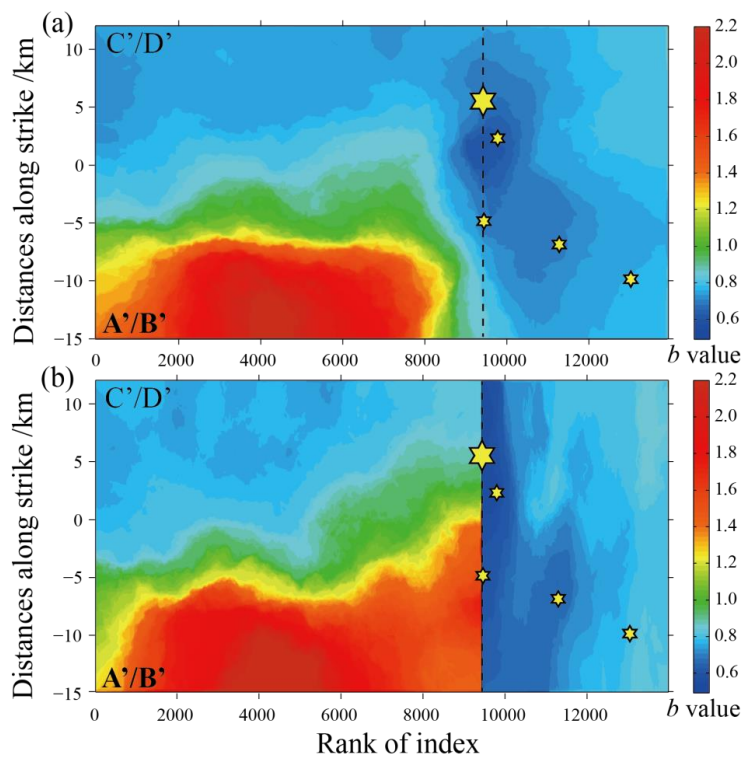
559  
560 **Fig. 4** The spatial distribution of the ensemble median  $b$  values of the best-100 solutions for  $N_c=2-40$  in the  
561 Changing area. (a) The ensemble median  $b$  values before the Changing  $M_s$  6.0 earthquake is  
562 distributed on the horizontal plane after the rotation; (b) The ensemble median  $b$  values obtained by  
563 calculation of all the earthquake including the aftershocks of the Changing  $M_s$  6.0 earthquake is  
564 distributed on the horizontal plane after the rotation; (c) distribution of the ensemble median  $b$  values  
565 before the occurrence of the Changing  $M_s$  6.0 earthquake in the rectangular frame A'B'C'D' on the  
566 depth profile; (d) distribution of ensemble median  $b$  values obtained by calculation of all earthquakes  
567 including aftershocks of the Changing  $M_s$  6.0 earthquake in the rectangular frame A'B'C'D' on the  
568 depth profile.



569  
570 **Fig. 5** The spatial distribution of the median absolute deviation (MAD) of the  $b$  values by the data-driven  
571 approach according to figure 4. (a) The ensemble MAD  $b$  values before the Changing  $M_s$  6.0  
572 earthquake is distributed on the horizontal plane after the rotation; (b) The ensemble MAD  $b$  values  
573 obtained by calculation of all the earthquake including the aftershocks of the Changing  $M_s$  6.0  
574 earthquake is distributed on the horizontal plane after the rotation; (c) distribution of the ensemble  
575 MAD  $b$  values before the occurrence of the Changing  $M_s$  6.0 earthquake in the rectangular frame  
576 A'B'C'D' on the depth profile; (d) distribution of ensemble MAD  $b$  values obtained by calculation of  
577 all earthquakes including aftershocks of the Changing  $M_s$  6.0 earthquake in the rectangular frame  
578 A'B'C'D' on the depth profile.



579

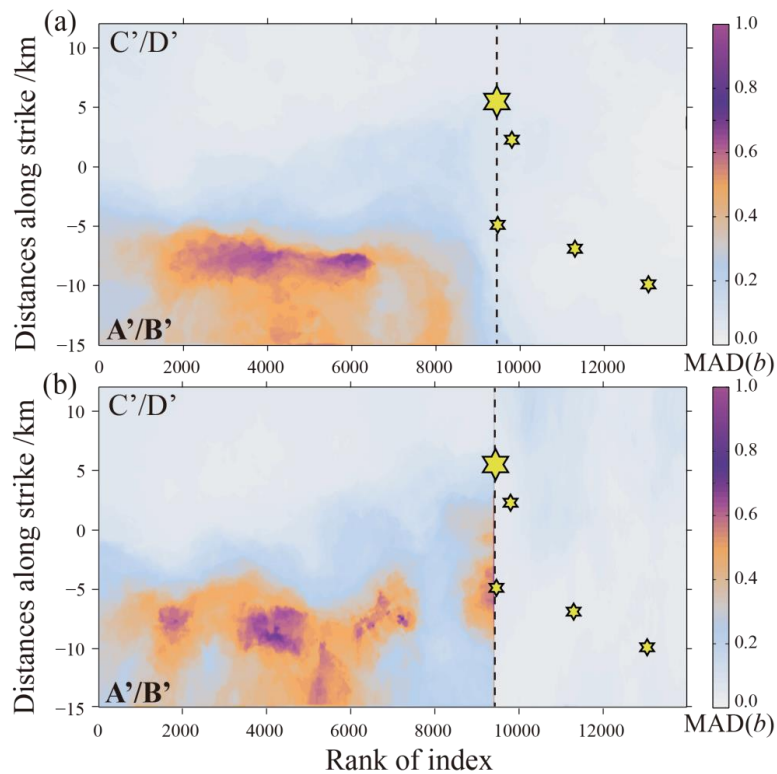


580

581 **Fig. 6** Spatiotemporal distribution of the ensemble median  $b$  values of the best-100 solutions for  $N_v=2-40$  on  
582 a 2-D space consisting of distance along strike and rank of index. (a) The ensemble median  $b$  values  
583 obtained from all data before and after the Changing  $M_s$  6.0 earthquake; (b) The ensemble median  $b$   
584 values obtained from the data before and after the Changing  $M_s$  6.0 earthquake, respectively. The  
585 vertical dotted line shows where the  $M_s$  6.0 earthquake occurred.



586



587

588

589

590

591

592

**Fig. 7** Spatiotemporal distribution of the median absolute deviation (MAD) of the  $b$  values of the best-100 solutions for  $N_s=2-40$  on a 2-D space consisting of distance along strike and rank of index. (a) The ensemble MAD  $b$  values obtained from all data before and after the Changning  $M_s 6.0$  earthquake; (b) The ensemble MAD  $b$  values obtained from the data before and after the Changning  $M_s 6.0$  earthquake, respectively. The vertical dotted line shows where the  $M_s 6.0$  earthquake occurred.